Chinese Chemical Letters 33 (2022) 4669–4674

Contents lists available at ScienceDirect

Chinese Chemical Letters

journal homepage: www.elsevier.com/locate/cclet

In situ localization of $BiVO_4$ onto two-dimensional MXene promoting photoelectrochemical nitrogen reduction to ammonia

Demei Zhang[a], Shiyu Yang[a], Xiaoyu Fang[a], Huifeng Li[a,*], Xuebo Chen[b,c,*], Dongpeng Yan[a,b,c,*]

[a] *Beijing Key Laboratory of Energy Conversion and Storage Materials, Key Laboratory of Radiopharmaceuticals, Ministry of Education, College of Chemistry, Beijing Normal University, Beijing 100875, China*
[b] *Key Laboratory of Theoretical and Computational Photochemistry, Ministry of Education, College of Chemistry, Beijing Normal University, Beijing 100875, China*
[c] *Green Catalysis Center, College of Chemistry, Zhengzhou University, Zhengzhou 450001, China*

ARTICLE INFO

Article history:
Received 26 November 2021
Revised 29 December 2021
Accepted 1 February 2022
Available online 7 February 2022

Keywords:
Photoelectrocatalysis
Nitrogen reduction reaction
$BiVO_4$
2D materials
MXene

ABSTRACT

The existing industrial ammonia synthesis usually adopts the Haber-Bosch process, which requires harsh conditions of high temperature and high pressure, and consumes high energy. Under this circumstance, photoelectrochemical (PEC) catalysis is regarded as a promising method for N_2 reduction reaction (NRR), but bears problems of low efficiency and yield. Thus, exploring active catalysts remains highly desirable. In this work, $BiVO_4$@MXene hybrids have been facilely synthesized by a hydrothermal route. The heterojunctions by the *in situ* growth of $BiVO_4$ onto two-dimensional (2D) MXene greatly increase the NRR efficiency: under photoelectric conditions, the optimized NH_3 yield is 27.25 µg h^{-1} cm^{-2}, and the Faraday efficiency achieves 17.54% at −0.8 V relative to the reversible hydrogen electrode (RHE), which are higher than most state-of-the-art NRR (photo) electrocatalysts. The mechanism speculation shows the enhanced light absorption range and the heterojunction formation largely promote the separation and the transfer efficiency of photogenerated carriers, thereby improving the PEC catalytic ability. Therefore, this work provides a hybrid route to combine the advantages of photo and electric catalysis for effective artificial nitrogen fixation.

Synthetic ammonia is a major breakthrough in the history of modern technology and has alleviated the problem of food shortages [1]. Ammonia has become one of the most produced chemical compounds in the world due to its wide range of uses, *e.g.*, more than 80% of the ammonia is used to make nitrogenous fertilizers [2]. Since 1913, the industrial ammonia synthesis has adopted the Haber-Bosch process [3]. With the advancement of technology and the renewal of equipment, the process conditions for industrial ammonia synthesis have been optimized. At present, the conversion rate of each reactant in industrial ammonia synthesis is between 25%–35%, depending on the design and configuration of the reactors [4,5]. There are still two problems to be solved: (1) The process needs to consume nearly 1.2% of the world's energy [6], including 5% of natural gas, because the raw material H_2 comes from steam reformed natural gas [7]; (2) The process emits 1.5% CO_2 gas in the atmosphere every year, which affects the environment and climate [8].

The electrocatalytic nitrogen reduction reaction (NRR) at room temperature and atmospheric pressure has zero emission in the whole process, and the raw material H^+ comes from an abundant aqueous solution [9–11]. In this context, electrocatalysis is very promising in the next generation of ammonia synthesis process. However, high bond energy and potential together with low yield and Faraday efficiency (FE) have limited the development of the electrocatalytic NRR to some extent. Thus, the design of new catalysts, which inhibit hydrogen evolution reaction (HER) activity to boost NRR process, is highly desirable [12–14]. From the view of clear energy, in photoelectrochemical (PEC) cells, semiconductor materials are usually used as photoelectrodes, which play an important role in light absorption and photocatalysis, and also effectively promote the electrocatalytic process with the aid of light [15,16]. It has been reported that the p-type semiconductor as photocathode can catalyze the NRR [17]. By modifying the surface state of the electrode, such as lattice defects and specific surface area, the PEC activity can be improved [18]. A typical PEC catalysis intro-

---

* Corresponding authors.
E-mail addresses: lihuifeng@bnu.edu.cn (H. Li), xuebochen@bnu.edu.cn (X. Chen), yandp@bnu.edu.cn (D. Yan).

https://doi.org/10.1016/j.cclet.2022.02.001

duces light energy to the electrocatalysis equipment [19,20], which combines advantages of photocatalysis and electrocatalysis to ensure commercial ammonia production [21]. The key to PEC NRR also includes selectively increase of the N_2 adsorption and effectively decrease of the activation energy barrier in each intermediate reaction.

In addition to the broadly applicable precious metals (such as Pt [22,23] and Au [24–26]), transition metals (including nickel [27,28], iron [29–32], cobalt [33], zinc [34], molybdenum [35,36] and bismuth [37–42]) systems also serve as NRR catalysts [43–46]. For example, the $BiVO_4$ catalyst with oxygen holes breaks the kinetic limit and promotes the adsorption and reduction potential of N_2. The amorphization helps to increase the activity relative to the crystalline counterpart of electrocatalytic NRR [47]. Due to the extremely low solubility of nitrogen in aqueous solutions, the adsorption of nitrogen at the surface of the catalyst becomes a difficulty [48]. The high specific surface area of two-dimensional (2D) materials, with effective electron transport channels and a large number of surface unsaturated atoms, can increase the catalytic active sites [49]. For example, the full exposure of edge in bismuth nanosheets and effective *p*-orbital electron delocalization facilitate the N_2 adsorption [50]. In addition, the semiconductor properties that limit the accessibility of surface electrons can improve the FE of the nitrogen fixation reaction [51].

Among the 2D catalysts, MXene has large specific surface area, excellent metallic conductivity, and large number of unsaturated atoms on the surface which can stably adsorb positive charges, but performs weak nitrogen fixation ability [52–55]. It has been reported that MXene can be combined with semiconductors to form a Schottky junction for efficient photocatalytic hydrogen evolution, because it can generate the built-in electric field to effectively improve carrier seperation [56,57]. In this work, we used acid etching to obtain 2D layered MXene, and then hydrothermally grew $BiVO_4$ on the surface of MXene *in situ*. The different ratios of $BiVO_4$@MXene led to tunable PEC NRR properties, with the optimized NH_3 yield of 27.25 μg h^{-1} cm^{-2} and FE of 17.54% at −0.8 V *vs.* RHE under photoelectric conditions. The high PEC performance can be related to the Schottky junction formed between $BiVO_4$ and MXene, in which the photogenerated electrons excited by light can promote charge transfer, and the electron transport channel built by the heterostructure can effectively reduce the resistivity of the catalysts. Thus, we propose that hybridization of electrocatalysts and photoactive semiconductors can serve as an efficient way to realize the high-efficiency catalytic nitrogen fixation utilizing both light and electric energy.

Titanium aluminum carbide (Ti_3AlC_2, 98%), bismuth(III) nitrate pentahydrate ($Bi(NO_3)_3{\cdot}5H_2O$, 99%), vanadium nitrate (NH_4VO_3, 99.5%), sodium hydroxide (NaOH, 99%), sodium dodecylbenzenesulfonate (SDBS, 95%), Nafion (5 wt%) were purchased from Beijing InnoChem Science & Technology Co., Ltd. Hydrofluoric acid (HF, 40%) and nitric acid (HNO_3, AR) were purchased from Beijing Tong Guang Fine Chemicals Company. All the reagents were used without additional purification. Deionized (DI) water (H_2O) were used in the research.

Firstly, 5 g of Ti_3AlC_2 was ball milled for 6 h to become the fine powder. Secondly, 1.2 g of the prepared Ti_3AlC_2 powder was corroded with 20 mL of 40 wt% HF solution for 24 h under stirring to completely remove the Al layer. Finally, the solution was rinsed with H_2O to remove unnecessary HF until the pH of the solution reached 5–6, and the residue was dried under vacuum at 80 °C for 24 h.

$BiVO_4$ nanoparticles were prepared by a hydrothermal method. Typically, 2.45 g of $Bi(NO_3)_3{\cdot}5H_2O$ and 0.58 g of NH_4VO_3 were dissolved in 10 mL of HNO_3 (4 mol/L) solution and NaOH (2 mol/L) solution, respectively. Then, 0.25 g of SDBS was added to the above two solutions under vigorous stirring. After stirring for 0.5 h, two solutions were mixed. 2 mol/L NaOH was added to adjust the pH to 7, and then the mixture was continuously stirred for 0.5 h. After that, the suspension was transferred to a 50 mL stainless steel autoclave lined with Teflon and placed in an oven at 200 °C for 3 h. After the autoclave was cooled to room temperature, the resulting bright yellow sample was centrifuged, washed several times with water and ethanol, and then dried at 100 °C for 4 h. $BiVO_4$@MXene samples were prepared in the same way, except that $Bi(NO_3)_3{\cdot}5H_2O$ and MXene were dissolved in 10 mL of HNO_3 (4 mol/L) solution. The molar ratio of $Bi(NO_3)_3{\cdot}5H_2O$ and NH_4VO_3 was 1:1, while SDBS were added in proportion to the weight of $BiVO_4$ and Mxene was added to obtain $BiVO_4$@MXene samples with weight ratios of 0:1, 1:5, 1:2, 1:1, 2:1, 5:1 and 1:0, respectively.

Before electrocatalytic and PEC measurements, 5.0 mg catalyst was dispersed in a mixed solution containing 800 μL deionized water, isopropanol (200 μL) and 30 μL Nafion solution (5.0 wt%). Ultrasound for at least 1 h produced a stable suspension. Next, 200 μL of the suspension was loaded on a carbon paper electrode with an area of 1×1 cm^2 and dried under ambient conditions to obtain a working electrode. All electrochemical measurements were tested by a potentiostat (CHI 660E) through a three-electrode system. The working electrode, reference electrode and counter electrode corresponded to carbon paper supported catalyst, Ag/AgCl saturated electrode and Pt wire electrode, respectively. Nafion 211 membrane was used after treatment. An open beaker containing a 0.1 mol/L HCl solution around the test equipment was used to keep the concentration of ambient ammonia in the solution below the detection limit to avoid the impact on ambient ammonia. Before each electrolysis, N_2 gas was slowly bubbled for at least 30 min until the N_2 was saturated. In addition, during the entire NRR electrolysis process, N_2 gas was continuously bubbled into the electrolyte 0.1 mol/L K_2SO_4 for 2 h. Under the applied potential of *iR* (*i* refers to the current, while *R* is the overall resistance, including contact resistance, charge-transfer resistance, and intrinsic resistance) compensation (95%), linear sweep voltammetry (LSV) was used with a rate sweep of 2 mV/s. The calibration of all potential measurements was based on the following Nernst equation (Eq. 1) [53]:

$$E(\text{RHE}) = E(\text{Ag/AgCl}) + 0.197\text{V} + 0.059\text{pH} \tag{1}$$

For PEC process, carbon paper supported catalyst, Ag/AgCl saturated electrode and Pt wire electrode were working electrode, reference electrode and counter electrode, respectively. Additional light illumination supplied by a 300 W Xe arc lamp (Newport Corporation) was fitted with an AM 1.5 G filter at the cathode of the electrolytic cell. According to the $C_{dl} = I_c/v$, we tested the electrochemical double-layer capacitance at a potential of −0.05 V to 0.25 V relative to the RHE, so as to compare the actual electrochemical active surface area (ECSA) of the catalyst. In the formula, C_{dl}, I_c and v are the double-layer capacitance of the catalyst (F/cm^2), charging current (mA/cm^2) and scan rate (10, 20, 40, 60, 80 and 100 mV/s), respectively. Electrochemical impedance spectroscopy (EIS) was obtained at a voltage of 1.8 V relative to RHE, with a frequency range of 0.01–100 kHz, and an amplitude of 5 mV/s [54].

The obtained NH_3 was determined by the indoxyl blue method. Usually, 2 mL electrolyte of electrochemical cell was taken from the cathode compartment. After that, 2 mL of 1 mol/L NaOH solution containing salicylic acid (5 wt%) and sodium citrate (5 wt%), 1 mL of 0.05 mol/L sodium hypochlorite (NaClO) and 0.2 mL of nitroferricyanide sodium ($C_5FeN_6Na_2O$,1 wt%) were added. After standing at room temperature for 2 h, the absorbance was measured using an ultraviolet-visible spectrophotometer. The produced indoxyl blue can be quantitatively measured by the equation conversion of the absorbance value at a wavelength equal to 655 nm. Using

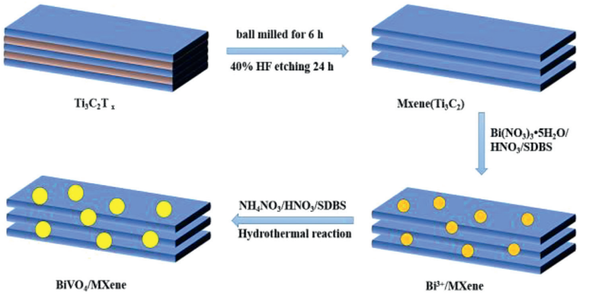

Scheme 1. Schematic diagram of the synthesis process of $BiVO_4$@MXene heterojunction.

standard NH_4Cl solutions with different concentrations, a standard curve was established in the K_2SO_4 electrolyte to obtain the calibration curve fitting equation required to calculate the NH_3 content.

The Watt and Chrisp method was used to measure the concentration of N_2H_4 in a 0.1 mol/L K_2SO_4 solution. We mixed 4 mL of the catalyzed electrolyte solution with an equal volume of color developer. The developer was a mixed solution of 4 g of *p*-(dimethylamine)benzaldehyde (*p*-$C_9H_{11}NO$) dissolved in concentrated HCl (15 mL) and anhydrous C_2H_5OH (150 mL). After standing for 0.5 h, we measured the absorbance of the yellow solution by the UV–vis spectrum at a wavelength of 455 nm. Finally, using the absorbance of standard hydrazine dihydrochloride solutions with different concentrations, a calibration fitting equation for calculating the N_2H_4 content can be established.

The yield of NH_3 can be determined by the formula: Yield rate = $(C(NH_3) \times V)/(t \times A)$, where $C(NH_3)$ is the measured NH_3 concentration, V is the electrolyte volume, t is the reaction time, and A is the surface area of the working electrode. FE is the percentage of electrons consumed during the formation of a given product, which is directly related to specific product selectivity. Assuming that three electrons are needed to generate an NH_3 molecule, the FE calculation formula is: $FE = (3F \times C(NH_3) \times V)/Q$.

50 mL of electrolyte solution obtained by PEC catalysis under −0.8 V with $^{14}N_2$ and $^{15}N_2$ gas was steamed respectively, until 5 mL of solution remained. 2 mL of concentrated sample, 2 mL of phenol solution (mixed with 6.0 g phenol, 3.0 g $Na_3PO_4 \cdot 12H_2O$, 3.0 g trisodium citrate dihydrate, 0.3 g of ethylenediaminetetraacetic acid anhydrous disodium salt, 0.02 g of $Na_2[Fe(CN)_5NO] \cdot 2H_2O$ in 100 mL solution), 1 mL NaClO solution (100 mL aqueous solution containing 2 mL of 5 wt% NaClO and 1.6 g of NaOH), and 1 mL of 0.5 wt% formic acid solution were mixed and stirred for 1 h. Then we used the LTQ-XL linear ion trap mass spectrometer from Thermo Scientific (USA) for further analysis.

The preparation of catalysts was based on the use of the 2D MXene material for the dispersion of the $BiVO_4$. HF acid etching was used to form a multilayer 2D MXene (Scheme 1), and then thermally combined with vanadium-bismuth metal salt to synthesize $BiVO_4$@MXene [58]. The hybrid catalysts with different proportions were hydrothermally synthesized to further optimize the PEC NRR performances.

Fig. 1a showed the XRD profiles of $BiVO_4$@MXene hybrids with different ratios (0:1, 1:5, 1:2, 1:1, 2:1, 5:1 and 1:0). In each case, the peak positions at 18.9°, 28.8° and 30.5° corresponded to the (011), (112) and (004) crystal planes of $BiVO_4$, respectively [59]. The diffraction peaks before 10° (dashed frame) were attributed to the MXene, which proved the effective combination between $BiVO_4$ and MXene [60]. It was observed that as the ratio of $BiVO_4$ increased, the main peak intensity of MXene decreased. The disappearance of the main peak of MXene occurred in the sample $BiVO_4$@MXene (5:1). The morphological characterizations of $BiVO_4$@MXene with different ratios were shown in Fig. S2 (Supporting information), which showed that the surface of MXene was gradually affected by the increase of $BiVO_4$. MXene was covered completely in the sample $BiVO_4$@MXene (5:1), which was consistent with the observation of XRD pattern. XPS was used to detect the element and valence changes in $BiVO_4$@MXene. As shown in Fig. 1b, all signals of Bi, V, O, C and Ti can be observed clearly in the survey XPS spectrum of $BiVO_4$@MXene. For the Ti 2p pattern (Fig. 1c), six peaks at 455.07, 456.24, 459.53, 460.97, 462.13 and 465.85 eV can be deconvoluted and ascribed to Ti(III) $2p_{3/2}$, Ti(II) $2p_{3/2}$, Ti(IV) $2p_{3/2}$, Ti(II) $2p_{1/2}$, Ti(III) $2p_{1/2}$ and Ti(IV) $2p_{1/2}$, respectively [57]. After combined with $BiVO_4$, the corresponding low-valence species disappeared and only two peaks corresponding to Ti(IV) $2p_{3/2}$ and Ti(IV) $2p_{1/2}$ can be observed, which may be due to some redox reaction occurred during the synthesis process. It is worth noting that the binding energy of Ti(IV) $2p_{3/2}$ and Ti(IV) $2p_{1/2}$ in $BiVO_4$@MXene had shifted negatively compared with MXene. Figs. 1d-f compared the valence changes of $BiVO_4$ after being combined with MXene. 164.02 eV and 158.82 eV represent the $4f_{5/2}$ and $4f_{7/2}$ of the Bi element, respectively, and 516.22 eV represents the $2p_{3/2}$ of the V element [61]. After combined with MXene to generate $BiVO_4$@MXene (1:1), binding energy of Bi 4f, V 2p and O 1s moved positively, which was opposite to that of Ti. Therefore, it can be inferred from the XPS characterization that the electron transfer path was from $BiVO_4$ to MXene, which indicated Schottky junction was formed in the $BiVO_4$@MXene composite [56].

The MXene synthesized by etching has been shown in Fig. 2a, from which an obvious layered structure can be observed. Fig. 2b showed that the side length of the single-layer MXene was about 150 nm and the thickness was 3 nm. For the composite (Figs. 2c and d), the $BiVO_4$ was uniformly dispersed on the surface and between layers of MXene in the $BiVO_4$@MXene (1:1). According to TEM image (Figs. 2e and f), $BiVO_4$@MXene had obvious crystalline and amorphous interface. The interplanar spacing of 0.226 nm corresponds to the (211) crystal plane of $BiVO_4$, and the amorphous section belonged to MXene. The element mapping (Figs. 2g-l) showed that the Bi, V, O, Ti, C and F elements were evenly distributed, which was consistent with XPS, indicating that $BiVO_4$ and MXene were tightly coupled together, forming a crystalline/amorphous Schottky junction.

Considering that K^+ ion can effectively block the collision probability between water molecules and the catalyst, and reduce the activity of the hydrogen evolution reaction (HER), the K_2SO_4 solution was selected as the electrolyte in this work. The calibration curve for calculating the yield was shown in Figs. S3 and S4 (Supporting information). From the LSV curve in Fig. S5 (Supporting information), it can be observed that the current curve of $BiVO_4$@MXene under photoelectric conditions was higher than the value without light, which indicated that $BiVO_4$@MXene hybrid was more active upon light irradiation. Fig. 3a showed the chronocurrent graph of $BiVO_4$@MXene (1:1) at different potentials, in which the more negative the potential, the greater the current value. Fig. 3b was the bi-coordinate diagram of ammonia yield and FE of $BiVO_4$@MXene, in which the NH_3 yield was 27.25 μg h^{-1} cm^{-2} and FE was 17.54% at −0.8 V *vs.* RHE. The stability of the catalyst was also tested. Fig. 3c showed the chronocurrent curve of $BiVO_4$@MXene under photoelectric condition in continuous 5 times at −0.8 V *vs.* RHE. Calculated from the UV absorption diagram (Fig. S7 in Supporting information), the NH_3 yield was relatively stable (Fig. 3d), and the specific values were shown in Table S1 (Supporting information). Under the same conditions at −0.8 V *vs.* RHE, the NH_3 yield and FE values of $BiVO_4$@MXene with different ratios (Fig. S6 in Supporting information) were 2.35, 2.94, 9.41, 14.90, 10.59, and 5.10 μg h^{-1} cm^{-2} and 0.40%, 1.93%, 5.20%, 11.87%, 5.11%, 1.11%, respectively. The yield (Fig. 4a) and FE (Fig. 4b) values of $BiVO_4$@MXene with various ratios showed a volcano

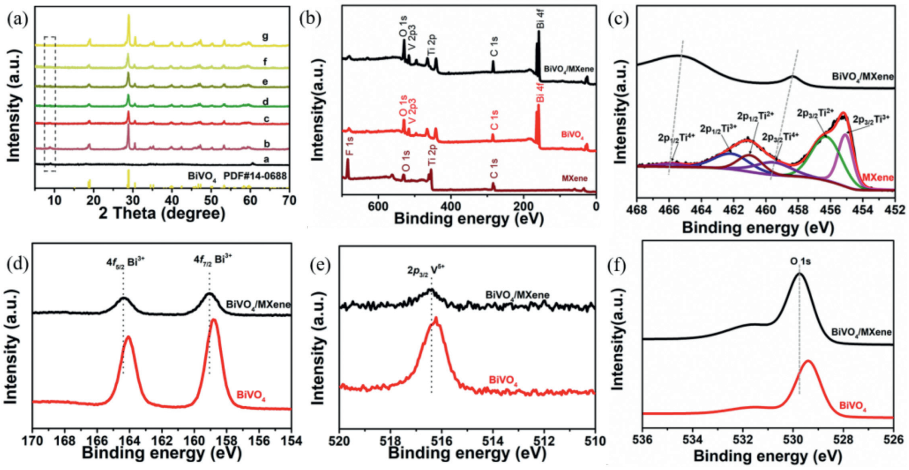

Fig. 1. (a) XRD diagrams of BiVO$_4$@MXene with different ratios (0:1, 1:5, 1:2, 1:1, 2:1, 5:1, 1:0) in curves a to g. (b) Survey XPS profile of as-prepared catalysts. (c) High-solution XPS spectra of Ti 2p of MXene and BiVO$_4$@MXene. (d) High-solution XPS spectra of Bi 4f. (e) V 2p and (f) O 1s of BiVO$_4$ and BiVO$_4$@MXene.

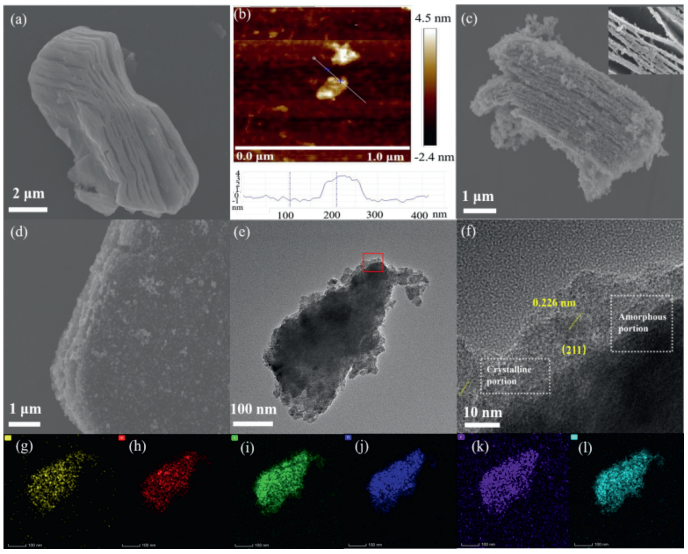

Fig. 2. (a) SEM and (b) AFM images of MXene. (c, d) SEM and (e) TEM images of BiVO$_4$@MXene (1:1). (f) The enlarged area of the selected area in (e). (g-l) The element mappings of Bi, V, O, Ti, C and F elements of BiVO$_4$@MXene (1:1).

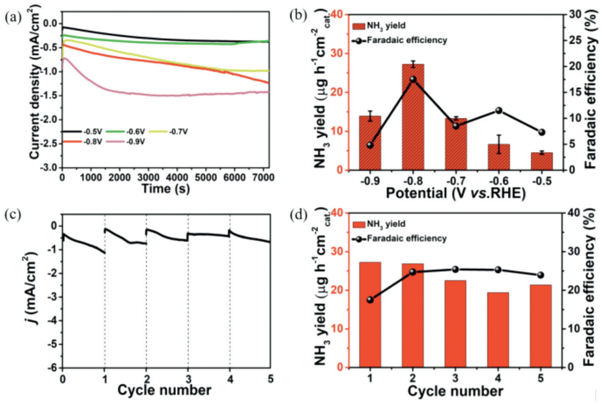

Fig. 3. (a) Chronocurrent graph. (b) Ammonia yield and FE of BiVO$_4$@MXene (1:1) under photoelectric conditions at different potentials. (c) Chronocurrent curve. (d) Ammonia yield and FE of BiVO$_4$@MXene with continuous 5 times under PEC condition at −0.8 V *vs.* RHE.

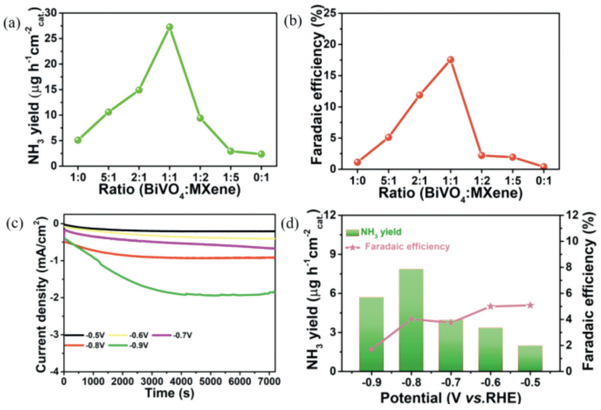

Fig. 4. (a) The NH$_3$ yields. (b) FE of various ratios under PEC condition at −0.8 V *vs.* RHE. (c) Chronocurrent curve. (d) NH$_3$ yield and FE of BiVO$_4$@MXene under no light condition.

pattern trend, in which BiVO$_4$@MXene (1:1) had the highest activity in PEC NRR. Upon removal of light, the chronocurrent curve (Fig. 4c) and low NH$_3$ yield (7.84 μg h^{-1} cm^{-2}) and FE (4.03%) values verified BiVO$_4$@MXene does exhibit high photoelectric activity (Fig. 4d). Such PEC performance can be further confirmed by the relatively low yield and FE of pristine MXene and BiVO$_4$ at −0.8 V *vs.* RHE (Table S2 in Supporting information).

In order to further explore the PEC mechanism, we explored the impact of the photoelectric response on the catalyst. As shown in Fig. 5a, under light irradiation, the photocurrent appeared instantaneously, but the photocurrent dropped instantly when turning off the light source. Moreover, the photocurrent value of BiVO$_4$@MXene was higher than that of the pristine BiVO$_4$ and MXene, which proved that the combination with MXene can effectively improve the light response of BiVO$_4$. Fig. 5b showed that photoelectron of BiVO$_4$@MXene had a much longer life span than BiVO$_4$, while that of MXene was almost negligible. The solid ultraviolet absorption pattern of BiVO$_4$@MXene (Fig. S9 in Supporting information) was converted into a semiconductor band gap (E_g) of 1.84 eV (Fig. 5c). Compared with BiVO$_4$ with a band gap of 2.22 eV, the band gap was reduced, which means BiVO$_4$@MXene can absorb a wider range of visible light. This also explained the higher photocurrent and photovoltage of BiVO$_4$@MXene. From XPS (Fig. S10 in Supporting information), valence band (E_{VB}) of BiVO$_4$ and BiVO$_4$@MXene was determined to be 1.94 and 1.38 eV, re-

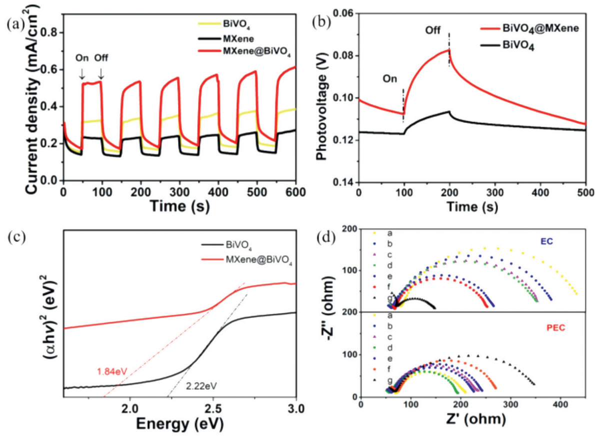

Fig. 5. (a) Photocurrent under light on and off conditions. (b) Photovoltage change dependent on the time. (c) Semiconductor band gap of the $BiVO_4$@MXene and pristine $BiVO_4$. (d) Nyquist diagrams of $BiVO_4$@MXene with different ratios (0:1, 1:5, 1:2, 1:1, 2:1, 5:1 and 1:0 for curves a-g) in 0.1 mol/L K_2SO_4 solution at 1.8 V *vs.* RHE with a frequency ranging from 0.1 Hz to 100 kHz with 5 mV/s.

spectively. The corresponding conduction band (E_{CB}) values were calculated to be −0.37 eV and −0.46 eV according to the formula $E_g = E_{VB} - E_{CB}$. The more negative of E_{VB} is, the more thermodynamically conducive to N_2 reduction. The emission intensity of $BiVO_4$@MXene in the fluorescence spectrum (Fig. S11 in Supporting information) was lower, which was attributed to the electron transfer through the heterojunction, thus reducing electron-hole recombination.

The charging current density difference Δj plot against scan rate of $BiVO_4$@MXene with different proportions was shown in Fig. S13 (Supporting information). As the content of MXene gradually increased, the slope became higher, which was consistent with the high surface area of 2D MXene material. Fig. 5d showed the Nyquist diagrams of the catalysts loaded on GCE in 0.1 mol/L K_2SO_4 solution at 1.8 V *vs.* RHE with the frequency ranging 0.1–100 kHz. The C_{dl} value can be calculated to represent the ECSAs. It can be seen that under light condition, the resistance of $BiVO_4$@MXene(1:1) was the lowest. The number of carriers in semiconductor is inversely proportional to the resistivity, so a high number of photogenerated electrons corresponds to a low resistivity. Moreover, mass spectrometry was used to prove the source of ammonia. As shown in Fig. S14 (Supporting information), 94.6% of phenol blue containing $^{14}N_2$ was detected in the $^{14}N_2$ electrolyte solution. Correspondingly, 75.0% of phenol blue containing $^{15}N_2$ was detected in the $^{15}N_2$ electrolyte solution. The results of mass spectrometry proved that ammonia was obtained from NRR catalytic process.

Based on the above experimental results, we confirm that as-synthesized $BiVO_4$@MXene has a superior PEC NRR performance. It was proved that V^{5+} provides the main adsorption and active sites due to its more negative adsorption energy in $BiVO_4$ [62,63]. However, if the numbers of photogenerated electrons is greater than those of N_2 adsorption and desorption, rest photogenerated electrons will recombine with holes, resulting in the loss of photogenerated electrons. We propose the PEC mechanism of $BiVO_4$@MXene as follows (Fig. 6): The localization of $BiVO_4$ is dispersed onto 2D MXene matrix, and the superior conductivity also enhances the electron transport ability. Under light irradiation, the photogenerated electrons from $BiVO_4$ can be transferred to MXene through the heterojunction interface. Then, N_2 is further reduced on the 2D surface of MXene, which greatly reduces the recombination probability of photogenerated electrons and holes. In addition, it adjusts the conductive band position of $BiVO_4$ to move it in the direction that is more conducive to light absorption, which improves the light response capability and the PEC NRR efficiency. In other words, $BiVO_4$ serves as the light response center for effective electron-hole separation, and MXene acts as the electrocatalytic active sites.

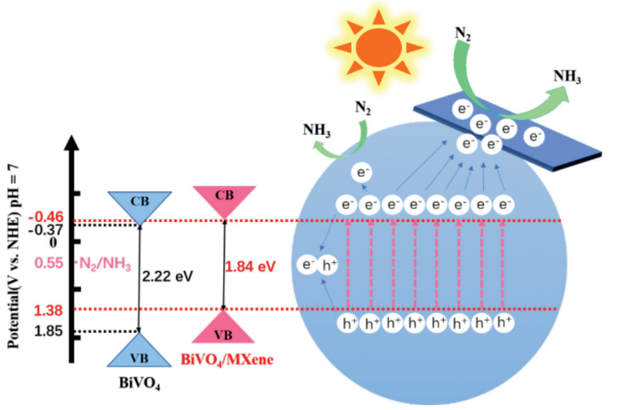

Fig. 6. Photoelectrocatalytic mechanism of N_2 to NH_3 by $BiVO_4$@MXene.

In summary, *in situ* growth of $BiVO_4$ onto 2D layered MXene results in the formation of uniform Schottky junction structure. The optimized NH_3 yield of $BiVO_4$@MXene (1:1) is 27.25 μg h^{-1} cm^{-2}, and the optimized FE is 17.54% at −0.8 V *vs.* RHE under PEC condition. Such NRR performances outperform most of state-of-the-art NRR electrocatalysts (Table S3 in Sopporting information). The photogenerated electrons excited by light can promote charge transfer, and the electron transport channel established by the heterojunction can effectively reduce the resistivity of the catalyst, thereby effectively improving the PEC NRR properties. Therefore, we propose a promising strategy to combine semiconductor $BiVO_4$ and high-conductivity MXene towards artificial nitrogen fixation application using primary energy solar energy.

Declaration of competing interest

The authors declare that they have no known competing financial interests or personal relationships that could have appeared to influence the work reported in this paper.

Acknowledgments

This work was supported by the National Natural Science Foundation of China (Nos. 21771021, 21822501, 21725303, 22061130206 and 22120102005), the Beijing Municipal Natural Science Fundation (No. JQ20003), the Newton Advanced Fellowship award (No. NAF\R1\201285), the Fok Ying-Tong Education Foundation (No. 171008), the Measurements Fund of Beijing Normal University, and the State Key Laboratory of Heavy Oil Processing.

Supplementary materials

Supplementary material associated with this article can be found, in the online version, at doi:10.1016/j.cclet.2022.02.001.

References

[1] V. Smil, Nature 400 (1999) 415.
[2] E. Matthews, Global Biogeochem. Cycles 8 (1994) 411–439.
[3] T. Xu, B.Y. Ma, J. Liang, et al., Acta Phys. Chim. Sin. 37 (2021) 2009043.
[4] M. Penkuhn, G. Tsatsaronis, Energy 137 (2017) 854–864.
[5] J.M. Herrera, G. Rubio, L.L. Haner, et al., Agronomy-Basel 6 (2016) 25.
[6] Y. Tanabe, Y. Nishibayashi, Coord. Chem. Rev. 257 (2013) 2551–2564.
[7] V. Smil, German, Isis 96 (2005) 310–312.
[8] F. Tanneberger, S. Abel, J. Couwenberg, et al., Mires and Peat 27 (2021) 05.

[9] D. Bao, Q. Zhang, F.L. Meng, et al., Adv. Mater. 29 (2017) 1604799.
[10] X.Y. Cui, C. Tang, Q. Zhang, Adv. Energy Mater. 8 (2018) 1800369.
[11] C.D. Lv, C.S. Yan, G. Chen, et al., Angew. Chem. Int. Ed. 57 (2018) 6073–6076.
[12] H. Cheng, L.X. Ding, G.F. Chen, et al., Adv. Mater. 30 (2018) 1803694.
[13] C. Lv, Y.M. Qian, C.S. Yan, et al., Angew. Chem. Int. Ed. 57 (2018) 10246–10250.
[14] L.L. Han, X.J. Liu, J.P. Chen, et al., Angew. Chem. Int. Ed. 58 (2019) 2321–2325.
[15] B. Oregan, M. Gratzel, Nature 353 (1991) 737–740.
[16] M. Gratzel, Nature 414 (2001) 338–344.
[17] X.G. Zheng, K. Taniguchi, A. Takahashi, et al., Appl. Phys. Lett. 85 (2004) 1728–1729.
[18] X.W. Cheng, Q.F. Cheng, X.Y. Deng, et al., Chemosphere 144 (2016) 888–894.
[19] J.H. Yang, D.G. Wang, H.X. Han, et al., Acc. Chem. Res. 46 (2013) 1900–1909.
[20] Y. Zhang, W.Q. Cui, W.J. An, et al., Appl. Catal. B: Environ. 221 (2018) 36–46.
[21] K. Ithisuphalap, H.G. Zhang, L. Guo, et al., Small Methods 3 (2019) 1800352.
[22] Z.G. Geng, Y. Liu, X.D. Kong, et al., Adv. Mater. 30 (2018) 1803498.
[23] H.C. Tao, C. Choi, L.X. Ding, et al., Chem 5 (2019) 204–214.
[24] Y. Yao, S.Q. Zhu, H.J. Wang, et al., J. Am. Chem. Soc. 140 (2018) 1496–1501.
[25] M. Nazemi, S.R. Panikkanvalappil, M.A. El-Sayed, Nano Energy 49 (2018) 316–323.
[26] Z.H. Xue, S.N. Zhang, Y.X. Lin, et al., J. Am. Chem. Soc. 141 (2019) 14976–14980.
[27] M. Arif, G. Yasin, W. Ye, et al., Appl. Catal. B: Environ. 265 (2020) 118559.
[28] M. Arif, G. Yasin, M. Shakeel, et al., J. Energy Chem. 58 (2021) 237–246.
[29] H.B. Wang, J.Q. Wang, R. Zhang, et al., ACS Catal. 10 (2020) 4914–4921.
[30] S.Z. Hu, X. Chen, Q. Li, et al., Appl. Catal. B: Environ. 208 (2017) 58–69.
[31] Y. Li, J.W. Li, J.H. Huang, et al., Angew. Chem. Int. Ed. 60 (2021) 9078–9085.
[32] Y. Li, Y. Kong, Y. Hou, et al., ACS Sustainable Chem. Eng. 9 (2019) 8853–8859.
[33] Y. Kong, Y. Li, B. Yang, et al., J. Mater. Chem. A 7 (2019) 26272–26278.
[34] Y. Kong, Y. Li, X.H. Sang, et al., Adv. Mater. 33 (2022) 2103548.
[35] W. Ye, M. Arif, X.Y. Fang, et al., ACS Appl. Mater. Interfaces 11 (2019) 28809–28817.
[36] M.A. Mushtaq, M. Arif, X.Y. Fang, et al., J. Mater. Chem. A 9 (2021) 2742–2753.
[37] H. Li, J. Shang, Z.H. Ai, et al., J. Am. Chem. Soc. 140 (2018) 526-526.
[38] H. Li, J. Shang, J.G. Shi, et al., Nanoscale 8 (2016) 1986–1993.
[39] S.Y. Wang, X. Hai, X. Ding, et al., Adv. Mater. 29 (2017) 1701774.
[40] S.L. Bai, H.M. Chu, X. Xiang, et al., Chem. Eng. J. 350 (2018) 148–156.
[41] X.T. Yang, Y.F. Ma, Y. Liu, et al., ACS Appl. Mater. Interfaces 13 (2021) 19864–19872.
[42] M. Liu, Y. Suzuki, Current Nanosci. 11 (2015) 499–503.
[43] M. Minakshi, M.G. Blackford, Mater. Chem. Phys. 123 (2010) 700–705.
[44] J. Han, X.Q. Ji, X. Ren, et al., J. Mater. Chem. A 6 (2018) 12974–12977.
[45] B.H.R. Suryanto, D.B. Wang, L.M. Azofra, et al., ACS Energy Lett. 4 (2018) 430–435.
[46] K. Liu, J.W. Fu, L. Zhu, et al., Nanoscale 12 (2020) 4903–4908.
[47] J.X. Yao, D. Boo, Q. Zhang, et al., Small Methods 3 (2019) 1800333.
[48] A.L. Krasilshchikov, L.G. Antonova, Z.M. Biryukova, et al., Zh. Fiz. Khim. 37 (1963) 204–206.
[49] X.X. Zhang, T.W. Wu, H.B. Wang, et al., ACS Catal. 9 (2019) 4609–4615.
[50] L.Q. Li, C. Tang, B.Q. Xia, et al., ACS Catal. 9 (2019) 2902–2908.
[51] Y. Wang, M.M. Shi, D. Bao, et al., Angew. Chem. Int. Ed. 58 (2019) 9464–9469.
[52] H.Y. Li, S.Q. Wei, H.X. Wang, et al., J. Colloid Interface Sci. 588 (2021) 1–8.
[53] J.L. Qu, J.W. Xiao, H.T. Chen, et al., Chin. J. Catal. 42 (2021) 288–296.
[54] C.Y. Wen, X.Z. Zheng, X.Y. Li, et al., Chem. Eng. J. 409 (2021) 128102.
[55] X.Y. Li, C.Y. Wen, H.F. Li, et al., J. Energy Chem. 47 (2020) 272–280.
[56] T. Cai, L.L. Wang, Y.T. Liu, et al., Appl. Catal. B: Environ. 239 (2018) 545–554.
[57] R. Xiao, C.X. Zhao, Z.Y. Zou, et al., Appl. Catal. B: Environ. 268 (2019) 118328.
[58] F. Shahzad, M. Alhabeb, C.B. Hatter, et al., Science 353 (2016) 1137–1140.
[59] T.W. Kim, K.S. Choi, Science 343 (2014) 990–994.
[60] J. Yan, C.E. Ren, K. Maleski, et al., Adv. Funct. Mater. 27 (2017) 1701264.
[61] L. Zhang, D.R. Chen, X.L. Jiao, J. Phys. Chem. B 110 (2006) 2668–2673.
[62] Y.J. Bai, J.M. Lu, H.Y. Bai, et al., Chem. Eng. J. 414 (2021) 128773.
[63] X.F. Long, L.L. Gao, F. Li, et al., Appl. Catal. B: Environ. 257 (2019) 117813.